Macromolecules

pubs.acs.org/Macromolecules Article

Membrane Pore Size Distribution by Design via Kinetic Engineering Using Initiated Chemical Vapor Deposition

Alexandra Khlyustova,[§] Yifan Cheng,[§] and Rong Yang*

Cite This: *Macromolecules* 2023, 56, 6492−6500 Read Online

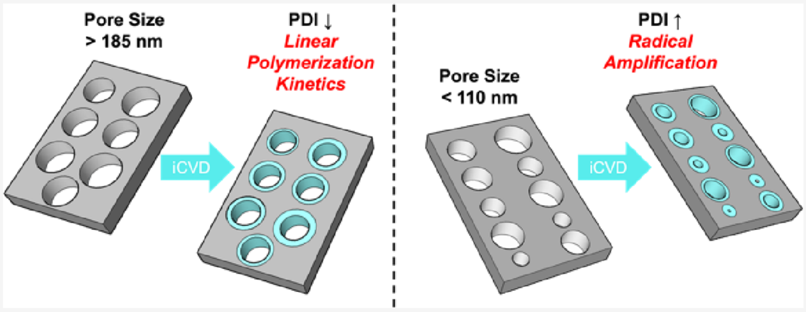

ABSTRACT: Membrane technology is one of the most cost-effective and clean separation techniques that are broadly adopted at the water-energy nexus and sustainable energy generation. While isoporous membranes are ideal for achieving high throughput and high purity simultaneously, manipulation of the pore size distribution has been laborious and often prohibitively costly for eventual deployment. In this study, we took a distinct approach to manipulate the pore size distribution by leveraging a conformal coating technique, namely, initiated chemical vapor deposition. This report provides a framework to understand heterogeneous polymerization under nanoconfinement as well as a facile approach for manipulating the pore size distribution in nanoporous membranes, which have the potential to enable advanced membranes that break through the permeability—selectivity tradeoff limit.

■ INTRODUCTION

Membrane separation is an effective, efficient, and versatile purification method with a small footprint.[1] It has been adopted in virtually every aspect of our modern life, ranging from gas separation[2] to chemicals production,[3] energy storage,[4] pharmaceutical manufacturing,[5] food processing,[6] and drug delivery.[7,8] A variety of materials have been used to fabricate porous membranes, including ceramics,[9] carbon nanotubes,[10] metal (e.g., palladium),[11] graphene,[12] etc., and polymers remain the most prevalent material in membrane fabrication due to their cost-effectiveness, ease of manufacturing and operation, and outstanding separation performance.[13−15] Controlling the pore size distribution of membranes has been a central topic in membrane science and polymer research, as the pore size distribution often dictates the membrane separation performance as described by the permeability and selectivity of a membrane. Despite the great variety of existing porous membranes, their performance is limited by a universal tradeoff between permeability and selectivity, which has been attributed to the polydispersed pore sizes where smaller pores restrict permeability and larger pores compromise selectivity.[13]

To manipulate the pore size distribution and thereby overcome that tradeoff in membrane performance, there have been sustained research efforts over the past few decades, including cocrystallization,[14] bio-inspired membrane designs (e.g., incorporating aquaporins into an impermeable polymer matrix),[15] mixed-matrix membranes,[16,17] self-assembled block copolymers,[18] among others. Despite the variety of approaches that have been devised, limited success has been achieved at scale. Existing porous membranes are commonly manufactured via solution casting[19] or non-solvent-induced phase separation,[20] which gives rise to a large polydispersity index (PDI) of the pores in a resulting membrane. While post-manufacturing surface modification of the existing membranes offers a scalable and cost-effective path toward narrowed or otherwise manipulated pore size distribution, there have been a few surface modification techniques that deliver the precision needed for engineering the pore size distribution.

Here, we employ an all-dry synthesis technique, namely, initiated chemical vapor deposition (iCVD), to achieve effective manipulation of the pore size distribution by tuning the deposition conditions (see Scheme 1a for the schematic of the iCVD reactor). The iCVD technology enables free-radical

Received: June 2, 2023
Revised: July 25, 2023
Published: August 9, 2023

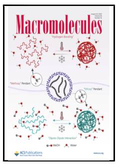

ACS Publications

https://doi.org/10.1021/acs.macromol.3c01078
Macromolecules 2023, 56, 6492−6500

Scheme 1. (a) Schematic of the Initiated Chemical Vapor Deposition (iCVD) Reactor with the Deposition Conditions Employed in This Work[a]; (b) Schematics of Post-deposition Effects on PDI with the Dominant Reaction Mechanisms (in Red Font) for Membranes with Pore Sizes >185 nm and <110 nm, Respectively[a]

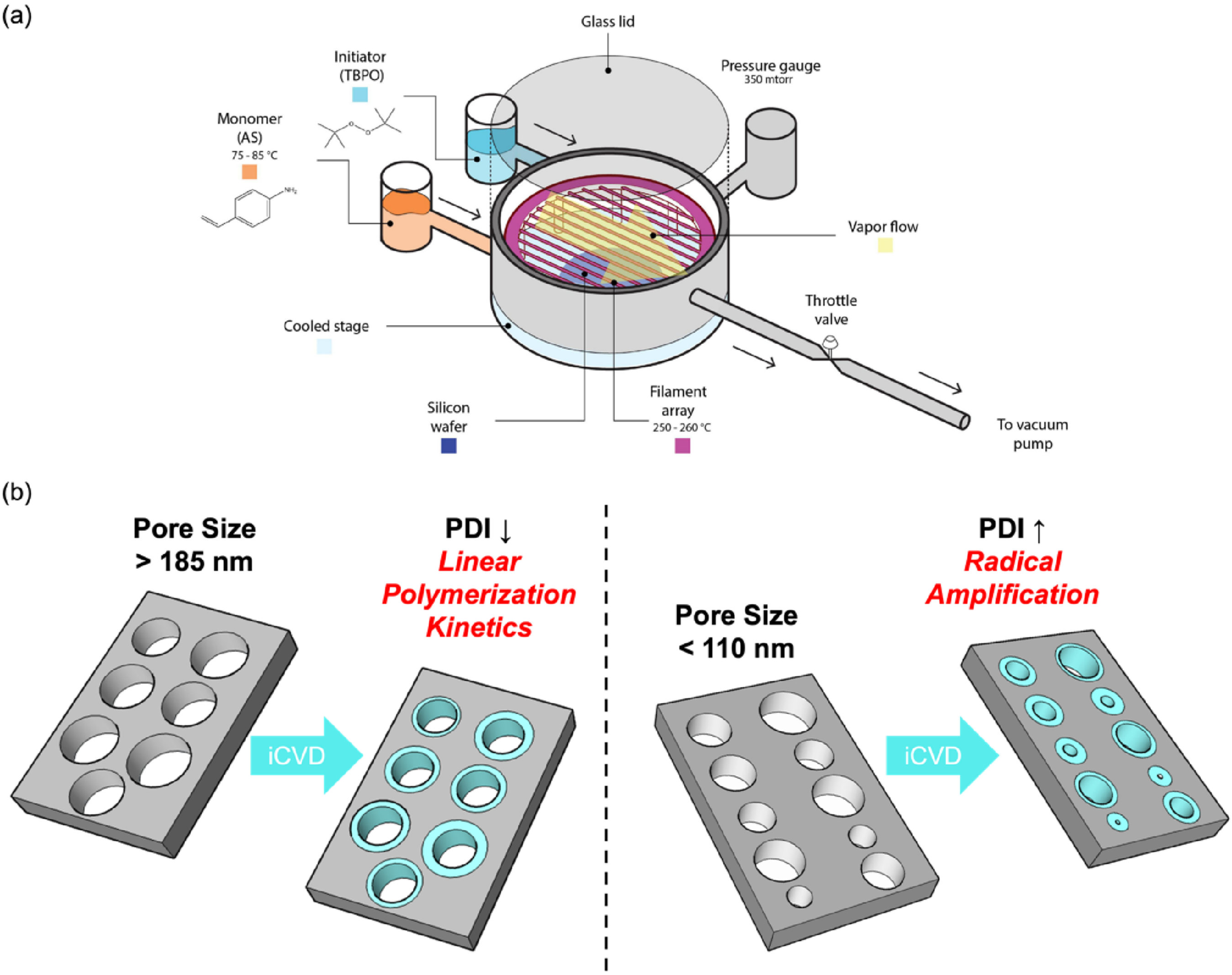

[a] Reproduced with permission from ref 39.

polymerization of vapor-phase precursors (i.e., initiator and monomers) at the surface of virtually any solid substrate without the need for a solvent.[21] It is uniquely suitable for the surface modification of porous membranes because it is conformal, meaning the polymer coating covers the geometry of the substrate with uniform thickness.[22] The conformal coverage results from Knudsen diffusion of radicals under the modest vacuum condition applied during iCVD, combined with a limited probability of radical impingement on the surface-adsorbed monomers to initiate chain propagation, i.e., a low sticking probability.[23] While the iCVD technology has been used to synthesize antifouling coatings on various porous and non-porous membranes,[24−27] previous investigations into the kinetics of iCVD polymerization under nanoconfinement have focused on the average pore size.[22,28] The effects of the coating technology on pore size distribution have not been investigated, a key knowledge gap that limits the impact of iCVD technologies in membrane science.

To fill that knowledge gap, this study systematically unravels the effects of synthesis conditions and the nanoconfinement dimensions on the resulting pore size distribution, using anodic aluminum oxide (AAO) membranes as a demonstration. Poly(4-aminostyrene) (PAS) was selected as the coating chemistry because the primary amine group allows secondary functionalization reactions to further boost membrane selectivity or fouling resistance (e.g., by immobilizing an enzyme).[29,30] Membranes with initial average pore sizes ranging from 80 to 185 nm were used. These pore sizes are representative of ultrafiltration (pore size <100 nm and > 20 nm) and microfiltration (pore size >100 nm) membranes. In recent years, ultra- and microfiltration membranes have garnered much attention as they play a crucial role in the essential purification and concentration processes in a wide range of industries, including pharmaceutical manufacturing during upstream and downstream processing,[31] food processing,[32,33] water purification,[34] renewable energy,[35] and environmental sustainability.[36]

Using this model system, we illustrate disparate effects of the iCVD coating on the pore size distributions of membranes with different initial average pore sizes. Those effects are tunable by adjusting the deposition conditions, such as the monomer partial saturation pressure (P_m/P_{sat}) of 0.06, 0.13, and 0.22. Specifically, a 30 nm iCVD coating reduced the PDI by up to 49% among 185 nm (initial diameter) pores, with the reduction of PDI increasing with the P_m/P_{sat}; we observed unchanged PDI among 110 nm (initial diameter) pores and increased PDI (up to 52-fold) among 80 nm (initial diameter) pores. Hence, our study represents a pioneering achievement in effectively manipulating pore size distribution, breaking new ground as previous research invariably concentrated on average pore size. Little is known about the effects of coating application on pore size distribution despite its importance in defining the separation performance of porous membranes.[37,38] This report bridges that knowledge gap by providing a framework to understand heterogeneous polymerization under nanoconfinement. It also introduces a new methodology to characterize pore size distribution in a top-down fashion using scanning electron microscopy (SEM) and image analysis. The tunable distribution of pore sizes via iCVD represents a facile approach for manipulating the performance of nanoporous membranes, which have the potential to enable advanced membranes that break through the permeability−selectivity tradeoff limit.

■ EXPERIMENTAL SECTION

The PAS thin films were synthesized via iCVD to coat the pore wall of nanoscale pores without pore-clogging (e.g., due to undesirable surface tension effects). We chose three pore sizes in this study, i.e., 85, 110, and 185 nm, informed by previous reports on the effects of nanoconfinement on the iCVD polymerization kinetics.[22,28] Briefly, nanoconfinement with a length scale of ∼110 nm (e.g., a nanopore with a diameter of 110 nm) has been discovered to amplify the effective free radical concentration during iCVD at shallow depths (e.g., near the pore entrance). It has been shown that the amplification of free radicals switches the iCVD kinetics from a recombination/disproportionation-dominated regime, in which polymerization follows the kinetics that is linearly dependent on the surface monomer concentration and the square root of the radical concentration, to a primary-radical-termination-dominated regime, in which the polymerization kinetics depends quadratically on the monomer concentration.[39] As such, the nanoconfinement leads to a non-linear coating thickness profile in the longitudinal direction (e.g., a ‘necking’ phenomenon within a nanopore). By choosing the three pore sizes that are below, at, or above 110 nm, this study unravels the effect of nanoconfinement on the post-deposition pore size distribution in the context of the nanoconfined iCVD polymerization kinetics. To obtain the nanoporous membranes with the desired average pore sizes, we fabricated AAO membranes in-house, using a two-step anodization procedure adopted from the previous study.[40] The procedure is known to cause irregular morphology near the top surface of a fabricated membrane,[41] and thus we removed the top 500 nm of the anodized membrane using ion milling prior to the iCVD coating step.

The membranes were subsequently coated with PAS using a custom-built iCVD reactor as shown in Scheme 1a, and the deposition conditions are summarized in Table 1. The fractional saturation pressure of the monomer, i.e., P_m/P_{sat} is a critical parameter in iCVD, which is proportional to the surface monomer concentration (when $P_m/P_{sat} \leq 0.2$) according to the Brunauer−Emmett−Teller (BET) isotherm that has been commonly used to describe monomer adsorption in iCVD. While a low P_m/P_{sat} value (e.g., $P_m/P_{sat} < 0.1$) is considered to lead to more conformal coatings inside micrometer-scale structures,[42−45] a recent report revealed that the opposite is true inside nanoscale pores due to the radical amplification.[28] A high P_m/P_{sat} value (e.g., $P_m/P_{sat} > 0.1$) leads to rapid consumption of the radicals near the entrance via primary radical termination, hence limiting coating growth in the high P_m/P_{sat} regime and leading to more conformal coating. Building from these insights, we chose the P_m/P_{sat} values of 0.06, 0.13, and 0.22, which cover the range of values investigated in previous studies without entering the non-linear regime of the BET isotherm.[39]

Table 1. iCVD Synthesis Conditions for PAS Coatings on the AAO Membranes

set	F(TBPO) [sccm]	F(AS) [sccm]	total flow [sccm]	P_m/P_{sat}	coating thickness on silicon wafer [nm]	deposition rate on silicon wafer [nm/min]
1	0.47	0.04	0.51	0.06	38.61 ± 1.85	0.39
2	0.47	0.07	0.54	0.13	34.50 ± 1.82	1.23
3	0.47	0.15	0.62	0.22	39.76 ± 2.04	2.65

In each deposition, a silicon wafer is coated alongside the AAO membranes to enable real-time monitoring of the coating thickness using a laser interferometer. Note that we controlled the coating thickness on the silicon wafer to be consistent (i.e., ∼35 nm) across different AAO membranes and different P_m/P_{sat} values such that the smallest pores (i.e., 80 nm diameter) would not be clogged, after which point the coating thickness inside the nanopores is no longer correlated with the iCVD polymerization kinetics.

■ RESULTS AND DISCUSSION

Chemical Characterization. To confirm that PAS was successfully synthesized using iCVD, Fourier-transform infrared spectroscopy (FTIR) and X-ray photoelectron spectroscopy (XPS) were used to characterize the coating composition (Figure 1). The FTIR spectrum of the as-synthesized PAS (Figure 1a) was consistent with previous reports.[39,46] The PAS spectrum retained the characteristics vibrations of the N−H stretching at ∼3400 cm^{-1}, the C═C stretching in the benzene ring at 1618 cm^{-1}, the N−H bending of the primary amine at 1514 cm^{-1}, the C−N stretching in the region from 1271 to 1100 cm^{-1}, and the N−H out-of-plane bending at 825 cm^{-1}. The completeness of polymerization was confirmed via the absence of the vinyl vibration at ∼900 cm^{-1}, from ═CH and ═CH$_2$ bending.

The XPS survey scan (Figure 1b) further corroborated the successful obtainment of PAS using iCVD, as signified by the carbon and nitrogen peaks. Interestingly, an oxygen peak was also observed (∼7.96 at. %), which we attributed to the irreversible reaction between ambient water molecules and the primary amine group in PAS, as reported previously.[47] Trace amounts of silicon were also captured, which is a common contaminant on coated silicon wafer samples. Using the XPS survey scan, we calculated the ratio of carbon to nitrogen for the as-deposited PAS to be ∼8.8:1, which is reasonably close to the theoretical ratio of 8:1, especially given the prevalence of adventitious carbon.[46]

Analysis of Pore Size Distribution. Upon confirmation of the chemical composition of the iCVD PAS coatings, we analyzed the pore size distribution of the pristine and coated AAO membranes, with different starting diameters and different P_m/P_{sat} values (Figures 2−4). To obtain the pore size distribution, scanning electron microscopy (SEM) was performed on the pristine and coated membranes in a top-down fashion, and the SEM images were analyzed using ImageJ.

We also examined the pore size distribution at 250 nm down the nanopores to assess the effect of iCVD on pore size distribution when radical amplification is minimal. Ion-milling (AJA Ion Mill) was used to remove the top 250 nm layer of the

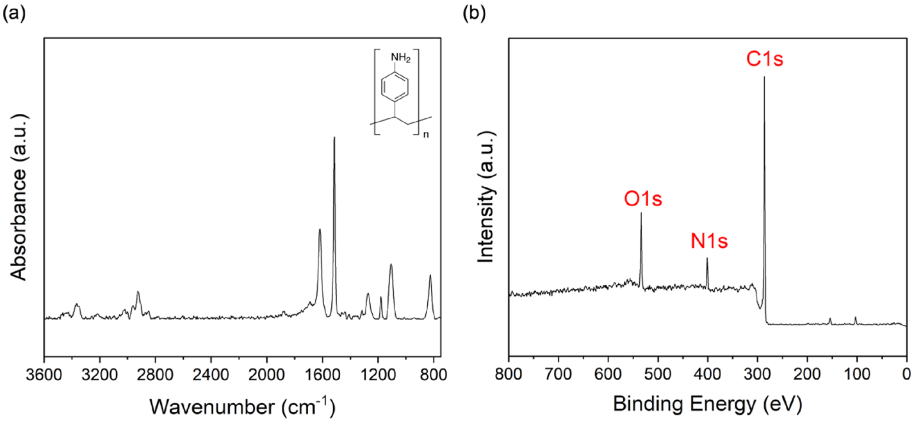

Figure 1. Chemical characterization of the PAS thin film synthesized using iCVD: (a) FTIR spectrum of the as-deposited PAS thin film and its molecular structure; (b) XPS survey scan of the as-deposited PAS.

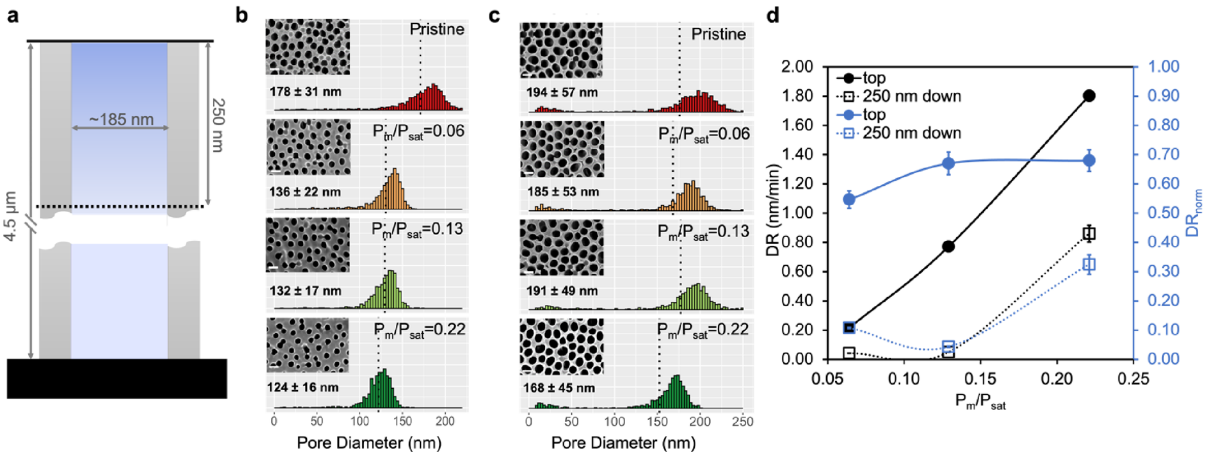

Figure 2. Pristine and iCVD-coated AAO membranes with an initial pore size of ∼185 nm, analyzed to illustrate the effect of iCVD coating, performed under different P_m/P_{sat} values, on the pore size distribution. (a) Schematic of a pristine AAO membrane with an average initial pore size of ∼185 nm. (b, c) Pore size distributions of pristine and coated AAO membranes at different P_m/P_{sat} values at (b) the top surface and (c) 250 nm down the pore. The scale bars represent 200 nm. The dotted lines signify the median of a pore size distribution; the average pore sizes and standard deviations are labeled on each panel ($n = 3$). (d) Deposition rate inside the nanopores (DR) (marked in black) and the DR normalized by the deposition rate on the silicon wafer (DR_{norm}) (marked in blue) on the top surface of coated AAO membranes and at 250 nm down the pores, obtained at three P_m/P_{sat} values.

pristine or coated AAO membranes. To eliminate the potential physical and chemical damage, ion milling was performed at a low acceleration voltage of 600 V with a grazing angle of 10°.[28,48] The membranes were subsequently imaged using SEM and analyzed using ImageJ, as detailed in the Materials and Experimental Methods section in the Supporting Information (Section 1, Table S1, and Figure S1).

Pore Size Distribution of 185 nm Membranes. The pore size distributions of pristine and iCVD-coated AAO membranes with an initial diameter of ∼185 nm are shown in Figure 2 (see Figures S2 and S3 in the Supporting Information for all SEM images used in the statistical analysis), with the dimensions of a pristine nanopore shown in Figure 2a. The pristine pore size, when imaged in a top-down fashion, was 178 ± 31 nm at the top surface of a membrane and 194 ± 57 nm at a depth of 250 nm into the pores (Figure 2b,c). That slight widening of the nanopores away from the top surface of an AAO membrane has been observed before in membranes fabricated using a similar protocol and can be explained by the different experimental procedures for the fabrication of 185 nm membranes as compared to 80−110 nm membranes (see Supporting Information, Section 1 for details).[49]

The iCVD of PAS was performed, using the P_m/P_{sat} values of 0.06, 0.13, and 0.22, respectively, until a ∼35 nm-thick coating was obtained on the silicon wafer that was placed next to the AAO membranes, as described above. Following the deposition, the average pore sizes decreased from 178 ± 31 nm (PDI = 0.031) to 136 ± 22, 132 ± 17, and 124 ± 16 nm, respectively, with P_m/P_{sat} values of 0.06, 0.13, and 0.22. The PDI values of the coated membranes were 0.027, 0.016, and 0.018, respectively, (Figure 5a), corresponding to 87%, 51%, and 56% of the pristine membranes. We observed similar reductions of the PDI values at the depth of 250 nm from the membrane top surface (Figure 2c), with the average pore sizes decreasing from 194 nm ± 57 nm (PDI = 0.087) to 185 ± 53 nm (P_m/P_{sat} = 0.06), 191 ± 49 nm (P_m/P_{sat} = 0.13), and 168 ± 45 nm (P_m/P_{sat} = 0.22), respectively, corresponding to PDI values of 0.080, 0.065, and 0.073 (Figure 5b). We attributed the effect of the iCVD coating to narrow the pore size distribution to a linear polymerization kinetics regime,[39] as discussed below.

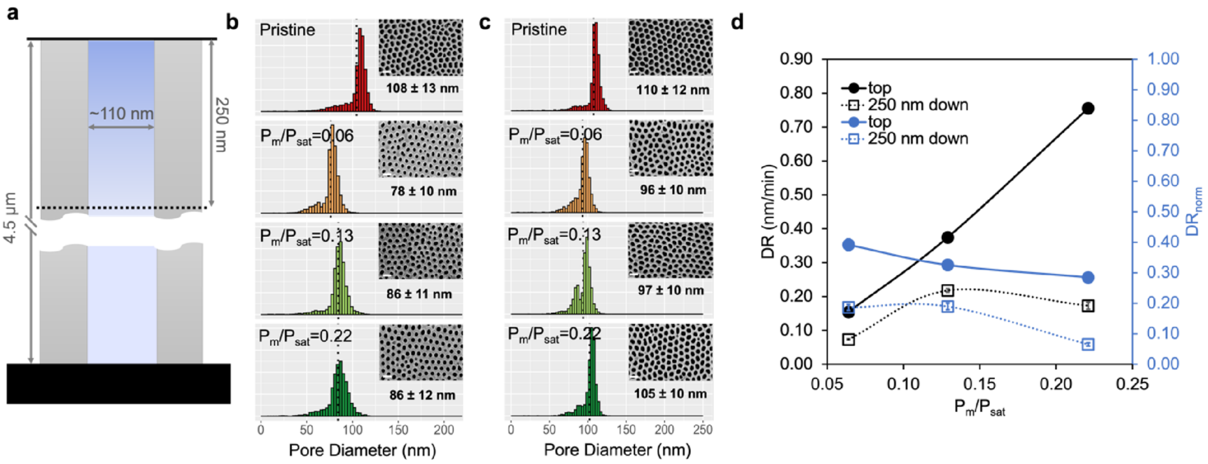

Figure 3. Pristine and iCVD-coated AAO membranes with an initial pore size of ∼110 nm, with their pore size distributions and deposition kinetics under nanoconfinement analyzed under different P_m/P_{sat} values. (a) Schematic of a pristine AAO membrane with an average initial pore size of ∼110 nm. (b, c) Pore size distributions of pristine and coated AAO membranes at different P_m/P_{sat} values at (b) the top surface and (c) 250 nm down the pore. The scale bars represent 200 nm. The dotted lines signify the median of a pore size distribution; the average pore sizes and standard deviations are labeled on each panel (*n* = 3). (d) DR inside the nanopores (marked in black) and the DR normalized by the deposition rate on the silicon wafer (DR_{norm}) (marked in blue) on the top surface of coated AAO membranes and at 250 nm down the pores, obtained at three P_m/P_{sat} values.

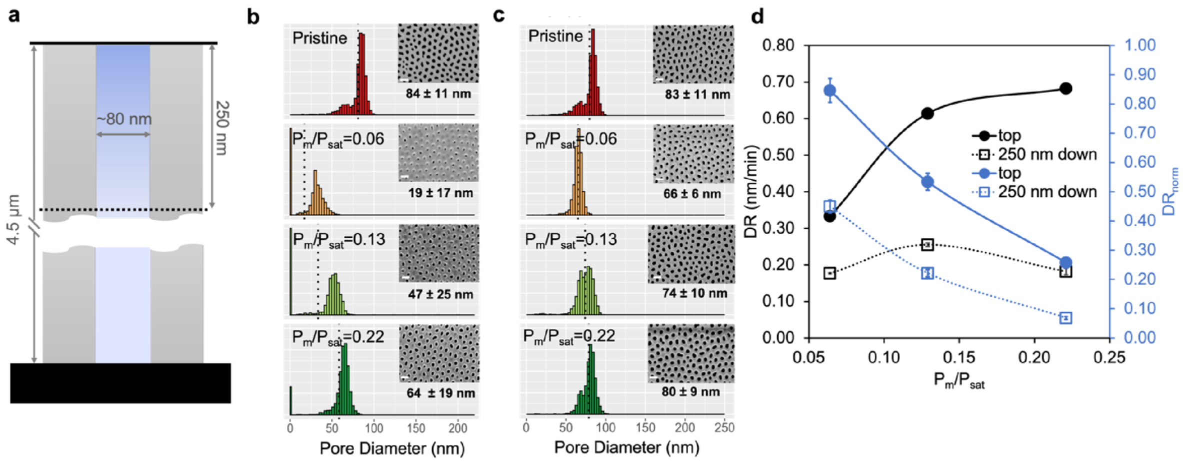

Figure 4. Pristine and iCVD-coated AAO membranes with an initial pore size of ∼80 nm, with their pore size distributions and deposition kinetics under nanoconfinement analyzed under different P_m/P_{sat} values. (a) Schematic of a pristine AAO membrane with an average initial pore size of ∼80 nm. (b, c) Pore size distributions of pristine and coated AAO membranes at different P_m/P_{sat} values at (b) the top surface and (c) 250 nm down the pore. The scale bars represent 200 nm. The dotted lines signify the median of a pore size distribution; the average pore sizes and standard deviations are labeled on each panel (*n* = 3). (d) DR inside the nanopores (marked in black) and the DR normalized by the deposition rate on the silicon wafer (DR_{norm}) (marked in blue) on the top surface of coated AAO membranes and at 250 nm down the pores, obtained at three P_m/P_{sat} values.

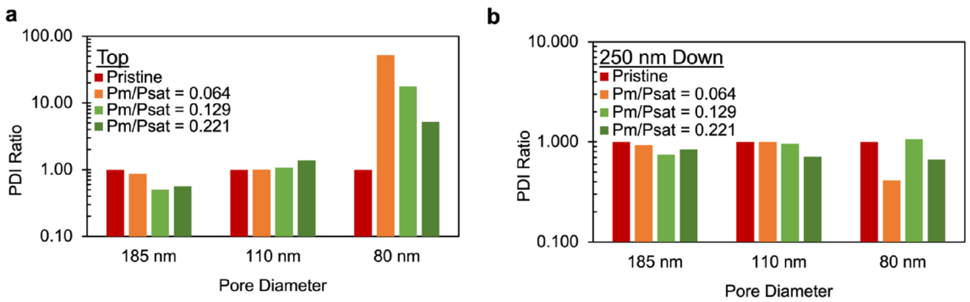

Figure 5. PDI ratio for AAO membranes with a pore diameter ranging from 80 to 185 nm at (a) the top surface and (b) 250 nm down the nanopores.

In the linear kinetics regime, the rate of polymerization and deposition is proportional to surface monomer concentration, hence P_m/P_{sat}. The DR, calculated using the pore sizes before and after the deposition and the deposition time, corroborated that linear rate dependence on the P_m/P_{sat} (Figure 2d, "top"). In the linear kinetics regime, the rate of polymerization is also proportional to the square root of the initiator concentration inside the nanopores. However, the initiator or radical concentration is not a simple function of the iCVD conditions. Although the flow rate of the initiator is controlled, the effective concentration of initiator/radicals inside the nanopores is also determined by the dimension of the nanoconfinement because the radical species have been shown to follow Knudsen diffusion in nanopores.[22,28,42] Indeed, under typical iCVD conditions, the molecular mean free path is on the order of 10 μm,[45] much greater than the pore sizes used here. As such, radicals travel down a nanopore by bouncing off the pore walls and initiation of polymerization occurs with a probability of ~0.0001−1%, which has been termed the sticking probability, Γ.[42] Therefore, when P_m/P_{sat} is kept constant, the rate of polymerization on the wall of nanopores is faster in larger pores and slower in smaller pores (as the flux of initiator radicals entering a pore is proportional to the cross-section area of the pore opening), hence narrowing the pore size distribution of a nanoporous membrane.

In addition to the DR at the top surface of the AAO membranes, we also analyzed the DR at 250 nm down from the surface (Figure 2d, "250 nm down") and calculated the normalized DR, i.e., DR_{norm}, defined as the DR measured on the AAO membranes divided by the DR on the silicon wafer (Figure 2d, blue lines). The DR at the top surface and 250 nm down from the surface of the AAO membranes follow similar trends within experimental error, hence supporting the similarly narrowed pore size distribution at both locations. A slight increase in DR_{norm} at the top surface was observed as we increased P_m/P_{sat}, which is consistent with the previously reported increase in the sticking probability as P_m/P_{sat} increases.[42,50,51] We refrain from drawing conclusions based on the trend in DR_{norm} at 250 nm down from the surface of the AAO membranes, as we suspect that the DR_{norm} value at the lowest P_m/P_{sat} used was dominated by the numerical instability.

Pore Size Distribution of 110 nm Membranes. The pore size distributions of membranes with a starting diameter of ~110 nm are shown in Figure 3 (see Figures S4 and S5 in the Supporting Information for all SEM images used in the statistical analysis), with the dimensions of a pristine nanopore shown in Figure 3a. The pristine pore size was 108 ± 13 nm at the top and 110 ± 12 nm at a depth of 250 nm down, respectively (Figure 3b,c). After iCVD deposition of ~35 nm PAS, the average pore size at the top decreased from 108 ± 13 nm (PDI = 0.015) to 78 ± 10 nm (PDI = 0.015), 86 ± 11 nm (PDI = 0.016), and 86 ± 12 nm (PDI = 0.021), respectively, with P_m/P_{sat} values of 0.06, 0.13, and 0.22 (Figures 3b and 5a). At a depth of 250 nm (Figure 3c), average pore sizes decreased from 110 ± 12 nm (PDI = 0.012) to 96 ± 10 nm (PDI = 0.012), 97 ± 10 nm (PDI = 0.011), and 105 ± 10 nm (PDI = 0.008) at P_m/P_{sat} = 0.06, 0.13, and 0.22, respectively (Figures 3c and 5b). Hence, the change in PDI was insignificant, and the effect of iCVD to narrow the pore size distribution was minimal at the average pore size of ~110 nm. While the DR inside 110 nm pores was lower than that inside 185 nm pores (Figures 2d and 3d), a similar linear dependence on P_m/P_{sat} was observed in both cases, indicating that the polymerization resides in the linear regime. The slower DR inside 110 nm pores was likely a result of the limited initiator flux into the nanopores, which was exacerbated by the reduced pore size (from an average of 185 to 110 nm). The DR_{norm} inside 110 nm pores exhibited a slightly decreasing trend with respect to P_m/P_{sat}, likely due to the limited diffusion of precursors into the nanopores, which became more pronounced as P_m/P_{sat} increased. As such, the DR_{norm} trend indicated that the sticking probability inside the 110 nm pores was lower than that inside the 180 nm pores.

That insignificant effect of iCVD coatings on the PDI of the 110 nm pores can be understood in the context of the aforementioned free radical amplification under nanoconfinement, which has been observed in nanopores with a diameter of ~110 nm.[28] Initiator amplification refers to an increment in the effective radical concentration under nanoconfinement due to frequent radical-surface collisions and a low sticking probability. The amplification effect has been shown to increase with decreasing pore sizes according to a previously established collision-based model.[22] This radical amplification effect, which increases in smaller pores, and the aforementioned flux of radicals entering a pore, which decreases in smaller pores, offset one another, leading to the less significant effect of iCVD on reducing the PDI of 110 nm pores compared to that on the 185 nm pores. The effect of radical amplification is lower at 250 nm down the pore compared to the top surface, thus likely contributing to the slightly decreased PDI of 110 nm pores at this depth.

Pore Size Distribution of 80 nm Membranes. Finally, the pore size distributions of pristine and PAS-coated membranes with an initial diameter of ~80 nm are shown in Figure 4 (see Figures S6 and S7 in the Supporting Information for all SEM images used in the statistical analysis), with the dimensions of an uncoated nanopore shown in Figure 4a. The uncoated pores had an average size of 84 ± 11 nm (PDI = 0.016) at the top surface and 83 ± 11 nm (PDI = 0.017) at 250 nm down the pore (Figure 4b,c). After the deposition of PAS, the average pore size at the top surface decreased to 19 ± 17 nm (P_m/P_{sat} = 0.06), 47 ± 25 nm (P_m/P_{sat} = 0.13), and 64 ± 19 nm (P_m/P_{sat} = 0.22), respectively, resulting in a drastic increase of PDI to 0.851 (52-fold), 0.291 (18-fold), and 0.086 (5-fold) as depicted in Figure 5a. This significant increase in the PDI and broadening of the pore size distribution can be explained by an extreme case of the aforementioned radical amplification effect inside the small pores of 80 nm diameter. Interestingly, the DR inside 80 nm pores (black circles in Figure 4d) was greater than the DR inside 110 nm pores (black circles in Figure 3d) at P_m/P_{sat} of 0.06 and 0.13. With the identical deposition conditions under each P_m/P_{sat} in mind, we attributed that greater DR to the considerably more significant radical amplification effect inside smaller pores. As the radical flux is a limiting factor in determining DR, the enhanced radical amplification inside 80 nm pores thus led to a greater rate of polymerization. In this radical-amplification-dominated regime, DR decreases with increasing pore size, thus leading to a broadened pore size distribution and larger PDI. At P_m/P_{sat} of 0.22, the DR inside the 80 nm pores was slightly less than the DR inside the 110 nm pores, which could be a result of the increased sticking probability at higher P_m/P_{sat}, which reduces the effective radical concentration and thus dampens the radical amplification effect inside smaller pores.

The effect of the deposition to broaden the pore size distribution was not observed at the depth of 250 nm into the pores. The coating resulted in a decrease of the average pore size from 83 ± 11 nm (PDI = 0.017) to 66 ± 6 nm (PDI = 0.007), 74 ± 10 nm (PDI = 0.019), and 80 ± 9 nm (PDI =

0.012), respectively, under the P_m/P_{sat} of 0.06, 0.13, and 0.22. The PDI values at this pore depth correspond to 41%, 106%, and 67% of the uncoated membrane (Figure 5b). This is consistent with the previous report that the radical amplification effect is most significant within the top 250 nm of a nanopore. Indeed, at the depth of 250 nm, the DR and DR_{norm} inside the 80 nm pores (Figure 4d, "250 nm down") followed similar trends to those observed inside the 110 nm pores (Figure 3d, "250 nm down") within experimental error, hence supporting the diminished effect of radical amplification at this pore depth.

While PAS is one of the several dozens of iCVD polymers reported to date, it is representative of the free-radical polymerization mechanism employed to synthesize those polymers. As such, we believe the reported framework is generalizable to other iCVD polymers, and it can be applied to predict the effects on pore size distribution based on the reactivity of the corresponding monomers. For example, a monomer with greater reactivity than AS is likely more prone to the radical amplification effect, which is anticipated to increase the PDI at a larger initial pore size than AS based on the reported framework. To confirm that prediction, iCVD was performed using two additional monomers, i.e., hydroxyethyl methacrylate (HEMA) and divinylbenzene (DVB). The former has a higher propagation constant than AS,[52] and the latter possesses two vinyl bonds, thus a greater probability of reaching the regime of radical amplification that leads to increased PDI. The polymers were deposited onto membranes with ~110 nm pores and compared to the PAS-coated membranes (see Table S2 for deposition conditions).

Consistent with the theoretical prediction, both polymers led to increased PDI inside 110-nm pores under all deposition conditions (Figure S8). A similar effect was observed for PAS but inside 80 nm pores, indicating that the greater propensity for radical amplification under nanoconfinement leads to an early onset of the pore-widening effect. PDVB increased the PDI from 0.015 to 0.083 at P_m/P_{sat} of 0.05 and to 0.044 at P_m/P_{sat} of 0.21. Similarly, PHEMA increased the PDI from 0.015 to 0.098 at P_m/P_{sat} of 0.06. and to 0.064 at P_m/P_{sat} of 0.19. These results further corroborate the generalizability of the theoretical framework to other monomers while highlighting the impact of the report in guiding the condition selection to obtain targeted post-deposition pore size distribution.

CONCLUSIONS

In conclusion, AAO membranes with pore diameters of 80, 110, and 185 nm (and a length of 4.5 μm) were coated with PAS using iCVD to understand the effect of all-dry polymerization under nanoconfinement on the pore size distribution.

The study revealed the critical role played by the phenomenon of initiator radical amplification under nanoconfinement in determining the post-modification pore size distribution. For ~185 nm membranes, the PDI narrows as the monomer partial saturation pressure (P_m/P_{sat}) increases, leading to a reduction of up to ~49% of the PDI of the nanopores. This was archived due to the dominance of the linear kinetics regime and insignificant radical amplification inside the 185 nm pores, where the deposition rate was shown to be proportional to membrane pore size. While the 110 nm membranes followed similar linear deposition kinetics, minimal change in the PDI was observed, indicating the presence of free radical amplification. Inside 80 nm pores, an increase of PDI by 52 times was observed, which was attributed to the strong radical amplification. The effect of radical amplification increases with decreasing pore size, thus leading to faster deposition inside smaller pores and broadened pore size distribution. That amplification effect has been reported to be minimal beyond the top 250 nm of a nanopore, and we thus examined the pore size distribution at 250 nm down the nanopores. At that depth, the 30 nm iCVD coating decreased the PDI slightly (by up to 25%) among the 185 nm pores and did not change the PDI of 110 nm and 80 nm pores, thus verifying the radical amplification effect on the PDI of nanopores.

Future studies will focus on testing the separation performance of these membranes and the development of theoretical models to allow the precise prediction of post-deposition membrane pore size based on P_m/P_{sat} and the initial pore size, which we identified as critical parameters determining the post-deposition PDI. These membranes with narrow pore size distribution and, hence, improved selectivity can make current separation processes more efficient and advance the field of membrane technology.

ASSOCIATED CONTENT

Supporting Information

The Supporting Information is available free of charge at https://pubs.acs.org/doi/10.1021/acs.macromol.3c01078.

Additional experimental details on the fabrication of AAO membranes, iCVD conditions, chemical characterization by FTIR and XPS, and pore size distribution analysis; the library of SEM top-surface images of PAS-coated membranes (PDF)

AUTHOR INFORMATION

Corresponding Author

Rong Yang – *Robert F. Smith School of Chemical & Biomolecular Engineering, Cornell University, Ithaca, New York 14853, United States*; orcid.org/0000-0001-6427-026X; Email: ryang@cornell.edu

Authors

Alexandra Khlyustova – *Robert F. Smith School of Chemical & Biomolecular Engineering, Cornell University, Ithaca, New York 14853, United States*; orcid.org/0000-0002-4313-5066

Yifan Cheng – *Robert F. Smith School of Chemical & Biomolecular Engineering, Cornell University, Ithaca, New York 14853, United States; Department of Food Science & Technology, Virginia Tech, Blacksburg, Virginia 24061, United States*

Complete contact information is available at: https://pubs.acs.org/10.1021/acs.macromol.3c01078

Author Contributions

[§]A.K. and Y.C. contributed equally to this work.

Notes

The authors declare no competing financial interest.

ACKNOWLEDGMENTS

This research was funded by the Department of Navy Office of Naval Research (ONR) grant N00014-20-1-2418 to R.Y. Y.C. is supported through USDA NIFA 2021-67034-35040 award. This work made use of the Cornell Center for Materials

Research (CCMR) Shared Facilities, which are funded through the NSF MRSEC program (DMR-1719875), and Cornell NanoScale Facility (grant number NNCI-2025233).

■ REFERENCES

(1) Park, H. B.; Kamcev, J.; Robeson, L. M.; Elimelech, M.; Freeman, B. D. Maximizing the Right Stuff: The Trade-off between Membrane Permeability and Selectivity. *Science* **2017**, *356*, 1138−1148.

(2) Koros, W. J.; Fleming, G. K. Membrane-Based Gas Separation. *J. Membr. Sci.* **1993**, *83*, 1−80.

(3) Waldburger, R. M.; Widmer, F. Membrane Reactors in Chemical Production Processes and the Application to the Pervaporation-Assisted Esterification. *Chem. Eng. Technol.* **1996**, *19*, 117−126.

(4) Wang, Y.; Chen, K. S.; Mishler, J.; Cho, S. C.; Adroher, X. C. A Review of Polymer Electrolyte Membrane Fuel Cells: Technology, Applications, and Needs on Fundamental Research. *Appl. Energy* **2011**, *88*, 981−1007.

(5) van Reis, R.; Zydney, A. Bioprocess Membrane Technology. *J. Membr. Sci.* **2007**, *297*, 16−50.

(6) Cui, Z. F.; Muralidhara, H. S. *Membrane Technology: A Practical Guide to Membrane Technology and Applications in Food and Bioprocessing*; Butterworth-Heinemann/IChemE, 2010.

(7) Strathmann, H. Membrane Separation Processes: Current Relevance and Future Opportunities. *AIChE J.* **2001**, *47*, 1077−1087.

(8) Khlyustova, A.; Cheng, Y.; Yang, R. Vapor-Deposited Functional Polymer Thin Films in Biological Applications. *J. Mater. Chem. B* **2020**, *8*, 6588−6609.

(9) Athayde, D. D.; Souza, D. F.; Silva, A. M. A.; Vasconcelos, D.; Nunes, E. H. M.; Da Costa, J. C. D.; Vasconcelos, W. L. Review of Perovskite Ceramic Synthesis and Membrane Preparation Methods. *Ceram. Int.* **2016**, *42*, 6555−6571.

(10) Wu, Y.; Liu, Z.; Ran, F. New Comprehensions on Structure Superiority of Asymmetric Carbon Membrane and Controlled Construction of Advanced Hierarchical Inner-Structure for High Performance Supercapacitors. *Microporous Mesoporous Mater.* **2019**, *275*, 14−25.

(11) Paglieri, S. N.; Way, J. D. Innovations in Palladium Membrane Research. *Sep. Purif. Methods* **2002**, *31*, 1−169.

(12) Garaj, S.; Hubbard, W.; Reina, A.; Kong, J.; Branton, D.; Golovchenko, J. A. Graphene as a Subnanometre Trans-Electrode Membrane. *Nature* **2010**, *467*, 190−193.

(13) Jiao, S.; Katz, L. E.; Shell, M. S. Inverse Design of Pore Wall Chemistry to Control Solute Transport and Selectivity. *ACS Cent. Sci.* **2022**, *8*, 1609−1617.

(14) Dai, X. L.; Li, S.; Chen, J. M.; Lu, T. B. Improving the Membrane Permeability of 5-Fluorouracil via Cocrystallization. *Cryst. Growth Des.* **2016**, *16*, 4430−4438.

(15) Kumar, M.; Grzelakowski, M.; Zilles, J.; Clark, M.; Meier, W. Highly Permeable Polymeric Membranes Based on the Incorporation of the Functional Water Channel Protein Aquaporin Z. *PNAS* **2007**, *104*, 20719−20724.

(16) Wang, X.; Chi, C.; Tao, J.; Peng, Y.; Ying, S.; Qian, Y.; Dong, J.; Hu, Z.; Gu, Y.; Zhao, D. Improving the Hydrogen Selectivity of Graphene Oxide Membranes by Reducing Non-Selective Pores with Intergrown ZIF-8 Crystals. *Chem. Commun.* **2016**, *52*, 8087−8090.

(17) Ma, X.; Kumar, P.; Mittal, N.; Khlyustova, A.; Daoutidis, P.; Mkhoyan, K. A.; Tsapatsis, M. Zeolitic Imidazolate Framework Membranes Made by Ligand-Induced Permselectivation. *Science* **2018**, *361*, 1008.

(18) Sun, W.; Wang, Z.; Yao, X.; Guo, L.; Chen, X.; Wang, Y. Surface-Active Isoporous Membranes Nondestructively Derived from Perpendicularly Aligned Block Copolymers for Size-Selective Separation. *J. Membr. Sci.* **2014**, *466*, 229−237.

(19) Ma, C.-H.; Yu, T. L.; Lin, H.-L.; Huang, Y.-T.; Chen, Y.-L.; Jeng, U.-S.; Lai, Y.-H.; Sun, Y.-S. Morphology and Properties of Nafion Membranes Prepared by Solution Casting. *Polymer (Guildf)* **2009**, *50*, 1764−1777.

(20) Wang, H. H.; Jung, J. T.; Kim, J. F.; Kim, S.; Drioli, E.; Lee, Y. M. A Novel Green Solvent Alternative for Polymeric Membrane Preparation via Nonsolvent-Induced Phase Separation (NIPS). *J. Membr. Sci.* **2019**, *574*, 44−54.

(21) Xu, J.; Gleason, K. K. Conformal Polymeric Thin Films by Low-Temperature Rapid Initiated Chemical Vapor Deposition (ICVD) Using Tert-Butyl Peroxybenzoate as an Initiator. *ACS Appl. Mater. Interfaces* **2011**, *3*, 2410−2416.

(22) Cheng, Y.; Khlyustova, A.; Chen, P.; Yang, R. Kinetics of All-Dry Free Radical Polymerization under Nanoconfinement. *Macromolecules* **2020**, *53*, 10699−10710.

(23) Baxamusa, S. H.; Im, S. G.; Gleason, K. K. Initiated and Oxidative Chemical Vapor Deposition: A Scalable Method for Conformal and Functional Polymer Films on Real Substrates. *Phys. Chem. Chem. Phys.* **2009**, *11*, 5227−5240.

(24) Yang, R.; Gleason, K. K. Ultrathin Antifouling Coatings with Stable Surface Zwitterionic Functionality by Initiated Chemical Vapor Deposition (ICVD). *Langmuir* **2012**, *28*, 12266−12274.

(25) Yang, R.; Goktekin, E.; Wang, M.; Gleason, K. K. Molecular Fouling Resistance of Zwitterionic and Amphiphilic Initiated Chemically Vapor-Deposited (ICVD) Thin Films. *J. Biomater. Sci., Polym. Ed.* **2014**, *25*, 1687−1702.

(26) Yang, R.; Jang, H.; Stocker, R.; Gleason, K. K. Synergistic Prevention of Biofouling in Seawater Desalination by Zwitterionic Surfaces and Low-Level Chlorination. *Adv. Mater.* **2014**, *26*, 1711−1718.

(27) Yang, R.; Xu, J.; Ozaydin-Ince, G.; Wong, S. Y.; Gleason, K. K. Surface-Tethered Zwitterionic Ultrathin Antifouling Coatings on Reverse Osmosis Membranes by Initiated Chemical Vapor Deposition. *Chem. Mater.* **2011**, *23*, 1263−1272.

(28) Cheng, Y.; Khlyustova, A.; Yang, R. All-Dry Free Radical Polymerization inside Nanopores: Ion-Milling-Enabled Coating Thickness Profiling Revealed "Necking" Phenomena. *J. Vac. Sci. Technol., A* **2022**, *40*, No. 033406.

(29) Khlyustova, A.; Kirsch, M.; Yang, R. Amphiphilic Copolymer Thin Films with Short Fluoroalkyl Side Chains for Antibiofilm Properties at the Solid-Liquid-Air Interface. *ACS Sustainable Chem. Eng.* **2022**, 15699−15713.

(30) Khlyustova, A.; Kirsch, M.; Ma, X.; Cheng, Y.; Yang, R. Surfaces with Antifouling-Antimicrobial Dual Function via Immobilization of Lysozyme on Zwitterionic Polymer Thin Films. *J. Mater. Chem. B* **2022**, *10*, 2728−2739.

(31) Lipnizki, F. Industrial Applications of Ultrafiltration in Pharmaceutical Biotechnology. *Eng. Life Sci.* **2005**, *5*, 81−83.

(32) Fernández García, L.; Alvarez Blanco, S.; Riera Rodríguez, F. A. Microfiltration Applied to Dairy Streams: Removal of Bacteria. *J. Sci. Food Agric.* **2013**, *93*, 187−196.

(33) Gerardo, M. L.; Zacharof, M. P.; Lovitt, R. W. Strategies for the Recovery of Nutrients and Metals from Anaerobically Digested Dairy Farm Sludge Using Cross-Flow Microfiltration. *Water Res.* **2013**, *47*, 4833−4842.

(34) Ma, J.; Guo, X.; Ying, Y.; Liu, D.; Zhong, C. Composite Ultrafiltration Membrane Tailored by MOF@GO with Highly Improved Water Purification Performance. *Chem. Eng. J.* **2017**, *313*, 890−898.

(35) Li, S.; Milia, M.; Schäfer, A. I.; Richards, B. S. Renewable Energy Powered Membrane Technology: Energy Consumption Analysis of Ultrafiltration Backwash Configurations. *Sep. Purif. Technol.* **2022**, *287*, No. 120388.

(36) Chew, C. M.; Aroua, M. K.; Hussain, M. A.; Ismail, W. M. Z. W. Evaluation of Ultrafiltration and Conventional Water Treatment Systems for Sustainable Development: An Industrial Scale Case Study. *J. Cleaner Prod.* **2016**, *112*, 3152−3163.

(37) Bowen, W. R.; Doneva, T. A. Atomic Force Microscopy Studies of Nanofiltration Membranes: Surface Morphology Pore Size Distribution and Adhesion. *Desalination* **2000**, *129*, 163−172.

(38) Yang, Q.; Chung, T. S.; Santoso, Y. E. Tailoring Pore Size and Pore Size Distribution of Kidney Dialysis Hollow Fiber Membranes

via Dual-Bath Coagulation Approach. *J. Membr. Sci.* **2007**, *290*, 153−163.

(39) Khlyustova, A.; Yang, R. Initiated Chemical Vapor Deposition Kinetics of Poly(4-Aminostyrene). *Front. Bioeng. Biotechnol.* **2021**, *9*, No. 670541.

(40) Masuda, H.; Fukuda, K. Ordered Metal Nanohole Arrays Made by a Two-Step Replication of Honeycomb Structures of Anodic Alumina. *Science* **1995**, *268*, 1466−1468.

(41) Chu, C. J.; Chung, P. Y.; Chi, M. H.; Kao, Y. H.; Chen, J. T. Three-Dimensional Block Copolymer Nanostructures by the Solvent-Annealing-Induced Wetting in Anodic Aluminum Oxide Templates. *Macromol. Rapid Commun.* **2014**, *35*, 1598−1605.

(42) Baxamusa, S. H.; Gleason, K. K. Thin Polymer Films with High Step Coverage in Microtrenches by Initiated CVD. *Chem. Vap. Deposition* **2008**, *14*, 313−318.

(43) Ozaydin-Ince, G.; Coclite, A. M.; Gleason, K. K. CVD of Polymeric Thin Films: Applications in Sensors, Biotechnology, Microelectronics/Organic Electronics, Microfluidics, MEMS, Composites and Membranes. *Rep. Prog. Phys.* **2012**, *75*, No. 016501.

(44) Coclite, A. M.; Howden, R. M.; Borrelli, D. C.; Petruczok, C. D.; Yang, R.; Yagüe, J. L.; Ugur, A.; Chen, N.; Lee, S.; Jo, W. J.; Liu, A.; Wang, X.; Gleason, K. K. 25th Anniversary Article: CVD Polymers: A New Paradigm for Surface Modification and Device Fabrication. *Adv. Mater.* **2013**, *25*, 5392−5423.

(45) Gleason, K. K. *CVD Polymers: Fabrication of Organic Surfaces and Devices*; Wiley-VCH Verlag GmbH & Co.: Weinheim, Germany, 2015; pp. 87−109.

(46) Xu, J.; Gleason, K. K. Conformal, Amine-Functionalized Thin Films by Initiated Chemical Vapor Deposition (ICVD) for Hydrolytically Stable Microfluidic Devices. *Chem. Mater.* **2010**, *22*, 1732−1738.

(47) Beauregard, N.; Al-Furaiji, M.; Dias, G.; Worthington, M.; Suresh, A.; Srivastava, R.; Burkey, D. D.; Mccutcheon, R. Enhancing ICVD Modification of Electrospun Membranes for Membrane Distillation Using a 3D Printed Scaffold. *Polymer* **2020**, *12*, 2074.

(48) Bassim, N. D.; De Gregorio, B. T.; Kilcoyne, A. L. D.; Scott, K.; Chou, T.; Wirick, S.; Cody, G.; Stroud, R. M. Minimizing Damage during FIB Sample Preparation of Soft Materials. *J. Microsc.* **2012**, *245*, 288−301.

(49) Pang, S. W.; Rathman, D. D.; Silversmith, D. J.; Mountain, R. W.; DeGraff, P. D. Damage Induced in Si by Ion Milling or Reactive Ion Etching. *J. Appl. Phys.* **1983**, *54*, 3272−3277.

(50) Petruczok, C. D.; Yang, R.; Gleason, K. K. Controllable Cross-Linking of Vapor-Deposited Polymer Thin Films and Impact on Material Properties. *Macromolecules* **2013**, *46*, 1832−1840.

(51) Ozaydin-Ince, G.; Gleason, K. K. Tunable Conformality of Polymer Coatings on High Aspect Ratio Features. *Chem. Vap. Deposition* **2010**, 100.

(52) Hamzehlou, S.; Reyes, Y.; Leiza, J. R. Detailed Microstructure Investigation of Acrylate/Methacrylate Functional Copolymers by Kinetic Monte Carlo Simulation. *Macromol. React. Eng.* **2012**, *6*, 319−329.